Chapter 5

Origin of zero thermal expansion in an average cubic structure in a Pb-free relaxor ferroelectrics

5.1 Introduction

Controlled thermal expansion driven thermal stability is a vital requirement for modern electronic devices *viz.*, solid oxide fuel cells, micropositioners, actuators, multi-layer ceramic capacitors, thin films, and many more [266, 267, 268, 269, 270, 271]. Thermal stability can be achieved using materials possessing Negative Thermal Expansion (NTE)/ Zero Thermal Expansion (ZTE). These materials include various types of structures such as open framework structures in ZrW_2O_8 [272] and ScF_3[273], magnetic structures in Fe–Ni invar alloys [274] and Mn_3Ge [275], superconductors *viz.*, MgB_2[276] and $NdFeAsO_{0.89}F_{0.11}$ [277], ferroelectric structures *viz.*, $PbTiO_3$[278, 279]and $Pb(Ti,V)O_3$ [280], non-polar disordered perovskites/Relaxor Ferroelectrics (RFEs) *viz.*, $Pb(Zn,Nb)O_3$ [281], $Pb(Fe,Nb)O_3$ [282], $Ba(Zr,Ti)O_3$ [283], and $Pb(Mg,Nb)O_3$ [260, 284] etc. Among these, NTE in perovskite (ABO_3) based ferroelectrics results from the strong covalent

character of A/B–O bonds, consequently leading to ferroelectrostriction [19]. For instance, materials such as $PbTiO_3$, $PbVO_3$, and $Pb(Ti,V)O_3$ with tetragonal structure at long-ranges exhibit high ferroelectrostriction due to strong covalent nature of Pb–O and Ti/V–O bonds, thereby resulting in NTE [19, 94, 280, 285]. Moreover, ferroelectrostriction observed in $BaTiO_3$ and $KNbO_3$ arises from the covalent character of Ti–O and Nb–O bonds respectively [94, 107, 157]. NTE can also be observed in technologically important non-polar disordered perovskites/RFEs due to cationic ordering, which can be achieved by temperature, pressure, frequency, and electric field [286, 287].

The synergistic coupling of RFEs with ZTE may lead to technologically important smart materials useful for various applications *viz.*, sensors & actuators, micropositioners, medical imaging devices, and many more [256, 288]. The relaxor materials exhibit broad and diffuse dielectric peaks for various frequencies [59, 137]. The diffuseness of dielectric peak in RFEs is due to the heterovalent substitution/ionic radii mismatch of cations, whereas the distribution of various Polar Nano Regions (PNRs) is responsible for frequency dispersion [117, 289]. The existence of PNRs has a significant influence on the lattice dynamics of relaxor ferroelectrics and can be attributed to the thermal behavior of materials [290, 291].

The relaxor properties are common to various oxide-based perovskites *viz.*, $Pb(Mg_{1/3}Nb_{2/3})O_3$, $Pb(Mg_{1/3}Nb_{2/3})O_3$-$x$$PbTiO_3$ [292], $Ba(Zr,Ti)O_3$-based ceramics [293], $K_{0.5}Na_{0.5}NbO_3$ (KNN50)- based ceramics *viz.*, KNN50-$x$$BaTiO_3$ (KNN50-xBT) [15], KNN50-$x$$(Ba,Sr)TiO_3$ (KNN50-xBST) [22, 62] etc [5, 130]. Among various RFE, Pb-based materials are widely studied for ZTE behavior [284]. Owing to detrimental effects of Pb, various Pb-free alternatives *viz.*, $Li_{0.2}Na_{0.8}NbO_3$ [166], KNN50 [249], etc., are being studied for their scientific and technological aspects [166, 249]. Among these, KNN50 is known to exhibit physical properties comparable to Pb-based materials [56, 249]. However, it does not exhibit relaxor properties. In a recent letter on $BaTiO_3$ doped KNN50 *viz.*,

KNN50-xBaTiO$_3$ (KBTx), Yang *et al.* have reported unique physical properties of the compositions exhibiting relaxor/diffuse properties [15]. Among various compositions, the dielectric response is maximum at ambient conditions for $x = 0.20$ [15]. Further, several authors doped Strontium (Sr) at A-site in KBTx to develop high-temperature Pb-free relaxor ferroelectrics useful for various applications *viz.*, aerospace, automotive, and many more [22, 62].

In the present chapter, we have selected $Ba_{0.9}Sr_{0.1}TiO_3$ (BST10) due to the maximum dielectric response [63, 64, 65, 66] and synthesized the solid solution of KNN50 with BST10 *viz.*, 0.80(KNN50)-0.20(BST10) (KBST20). The long- and short-range symmetries of KBST20 were determined using temperature-dependent neutron diffraction and Raman spectroscopy data, respectively. Temperature-dependent dielectric data and hysteresis loops were used to analyze the relaxor properties and expected ordering at low temperatures. The lattice parameters and volume were determined by Le Bail analysis. Further, the linear coefficient of thermal expansion [CTE (α_l)] and spontaneous volume ferroelectrostriction (SVFS) were calculated.

5.2 Experimental procedure

The 0.80($K_{0.5}Na_{0.5}NbO_3$)-0.20($Ba_{0.9}Sr_{0.1}TiO_3$)(KBST20) ceramics was prepared *via* conventional solid-state reaction route with raw chemicals *viz.*, K_2CO_3 (Sisco Research Laboratories Pvt. Ltd.) (99%), Na_2CO_3 (HIMIDEA Labs) (99.5%), $BaCO_3$ (HIMIDEA Labs) (99%), $SrCO_3$ (HIMIDEA Labs) (99%), Nb_2O_5 (HIMIDEA Labs) (99.9%), and TiO_2 (HIMIDEA Labs) (99%) dried at 393 K prior to weighing. The dried raw chemicals were weighed accordingly followed by milling for 24 hours. The milled powder was further calcined at 1173 K for 4 hours. The calcined powder is mixed with 2–5% PVA binder and was pelletized at 8-10 metric tons pressure. The pellets were further sintered at temperature of 1388 K for 3 hours. The neutron diffraction measurement was obtained from Institut

Laue-Langevin (ILL), Grenoble (λ = 1.28 Å). For dielectric and PE loop measurements, the silver electrodes were deposited on both sides of the pellets and the temperature-dependent dielectric measurement was performed using Keysight LCR meter with frequency and temperature range of 1 kHz–1 MHz and 105 K $\leq T \leq$ 650 K respectively. The PE loop measurement was conducted at 10 Hz frequency using Radiant Technology's Precision LCII Ferroelectric Tester. Further, temperature-dependent Raman spectra were acquired using a Horiba LabRAM HR Raman spectrometer with an Olympus BX41 microscope attachment. An excitation wavelength of 514.5 nm from a Lexel Model-95 argon ion laser was used. The samples were placed in a Linkam THMS600 microscope stage for variable temperature Raman measurements. The laser beam was focused onto the sample using a 50x LWD objective (N.A. = 0.50) and the backscattered light was dispersed *via* a 600 lines/mm grating onto a liquid nitrogen cooled CCD detector. The data was acquired using LabSpec v5 software. Laser power at the sample was approximately 0.4 mW. This value was checked to verify that no local heating effects from the laser beam occurred . The spectral range chosen for this study extended from 80 to 1900 cm^{-1}.

5.3 Result and discussion

5.3.1 Neutron Diffraction analysis

Temperature-dependent neutron diffraction data (9 K $\leq T \leq$ 500 K) were obtained from the D1B diffractometer at the Institut Laue-Langevin, Grenoble. The observed diffraction pattern shows the formation of a solid solution (see Fig. 5.1(a)). All reflections in the diffraction patterns exhibit a singlet nature, suggesting the cubic structure (see Figs. 5.1(b), 5.1(c), and 5.1(d)]. Owing to the singlet nature of the peaks, the diffraction patterns were refined with the $Pm\bar{3}m$ space group *via* Le Bail method. Moreover, the temperature-dependent Le Bail refinements were carried out for KBST20 ceramics (9 K$\leq T \leq$ 500 K)

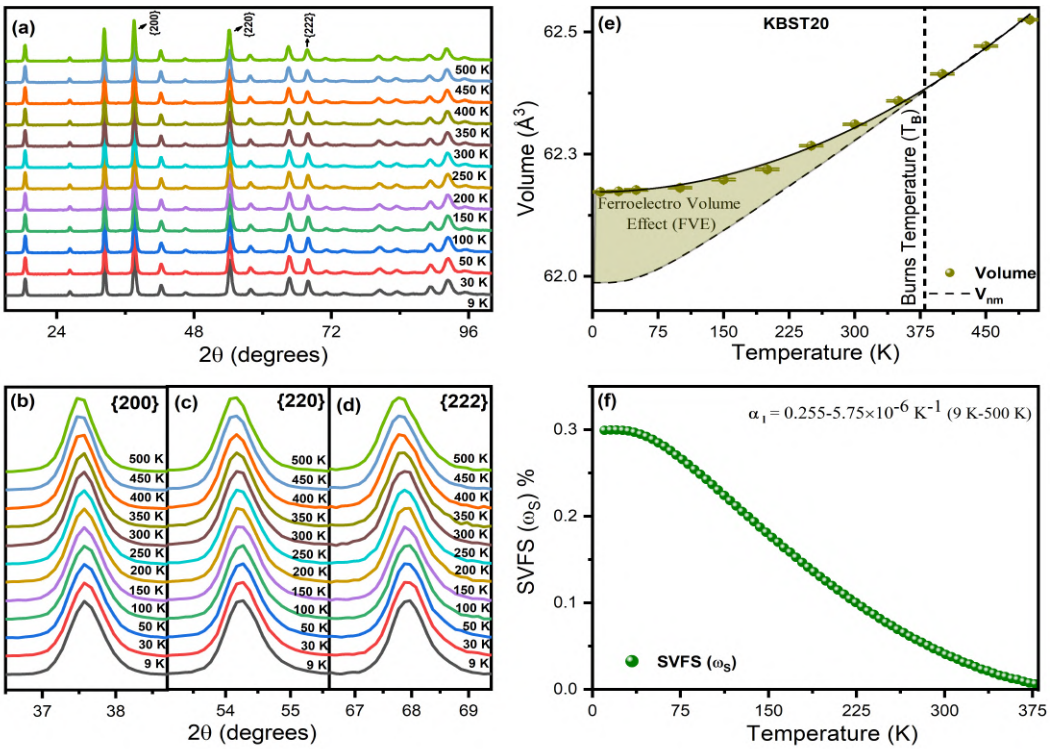

Fig. 5.1 (a) Temperature dependent neutron diffraction data of pure KBST20 ceramic for 9 K $\leq T \leq$ 500 K, (b), (c), (d) Temperature dependent evolution of {200}, {220}, and {222} peaks respectively for 9 K $\leq T \leq$ 500 K, (e) Temperature dependent variation of volume for KBST20 ceramic where the symbol represents the experimental volume, solid curve represents the polynomial fit of experimental volume, and dashed curve represents nominal volume obtained from fitting of Debye-Grüneisen equation for 380 K$\leq T \leq$ 500 K [17, 18, 19] and (f). Variation of SVFS (ω_s) with temperature for 9 K $\leq T \leq$ 380 K where SVFS has been calculated using interpolated volume data.

using FULLPROF [294] package. The Le Bail fitted profiles are shown in Fig. 5.2 with insets showing the fitted profiles of main perovskite peaks *viz.*, {200}, {220}, and {222}.

Figure 5.1(e) depicts the evolution of volume as a function of temperature. The volume shows nearly linear behavior above Burns temperature (T_B; determined from dielectric data) while it shows a non-linear behavior below T_B with a tendency to saturation at low temperatures below $\approx$ 100 K. Moreover, at low temperatures ($T \lesssim$ 100 K), the volume becomes nearly temperature-independent (see Fig. 5.1(e)), suggesting ZTE in

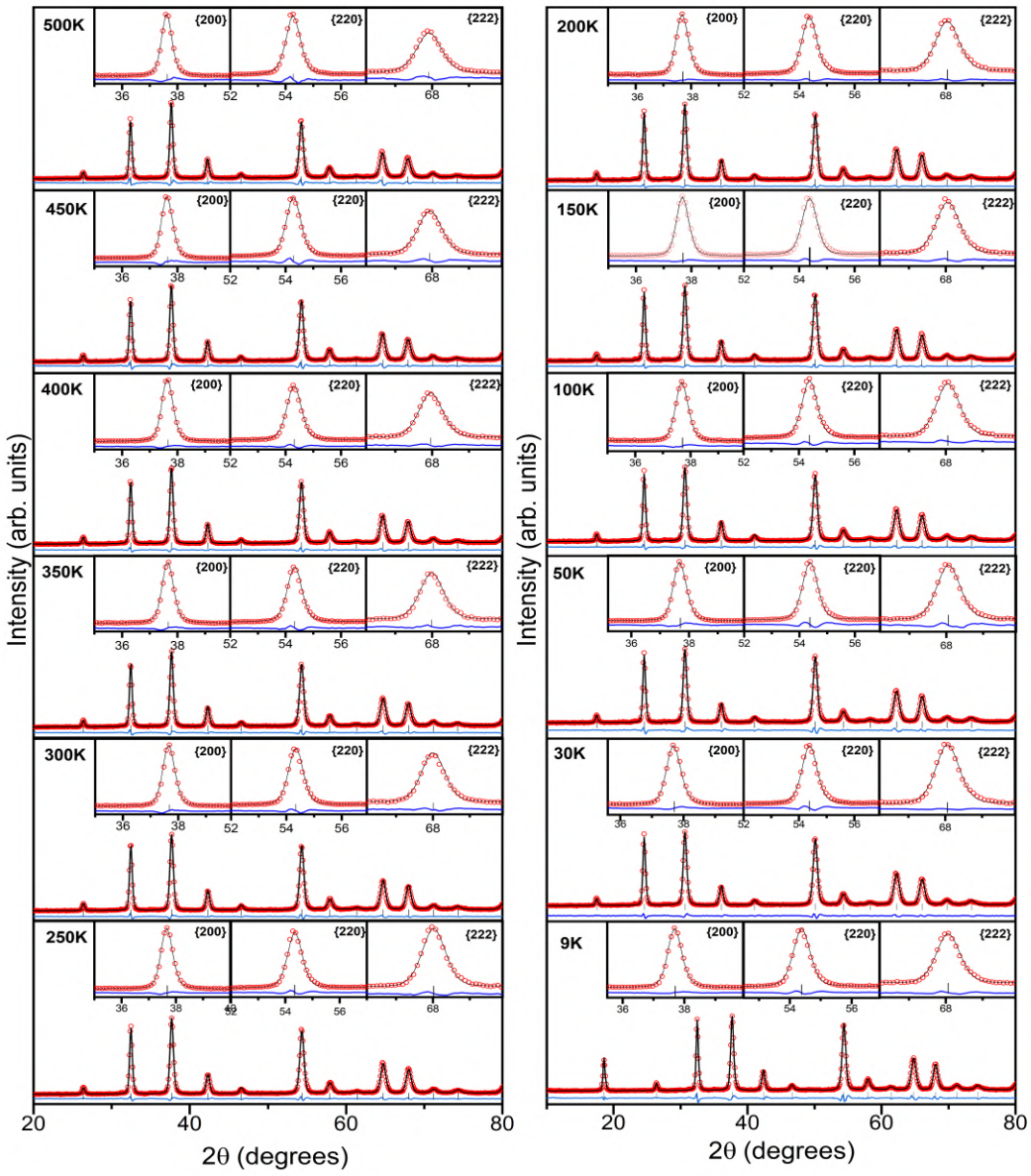

Fig. 5.2 Temperature-dependent Le Bail fits of KBST20 ceramics (9 K $\leq T \leq$ 500 K) with insets showing the fits of {200}, {220}, and {222} peaks. The continuous black line represents the simulated patterns while the open red circles represents the observed pattern. The Bragg reflections are represented by vertical black bars, and the continuous blue line at the bottom represents the difference between observed and simulated patterns.

the material. In order to quantify ZTE, we have calculated the volumetric coefficient of thermal expansion (α_V) using the following equation [19]:

$$\alpha_V = \frac{1}{V}\frac{\partial V}{\partial T} \tag{5.1}$$

where V is the volume at temperature T [17, 19]. For cubic systems, the linear α_l equals one-third of the volumetric α_V *i.e.*, $\alpha_l = \frac{1}{3}\alpha_V$ [19]. Here, for KBST20 ceramics, α_l and α_V ranges from 0.255-5.75 $\times 10^{-6}$ K^{-1} (9 K − 500 K) and 0.765-17.25 $\times 10^{-6}$ K^{-1} (9 K − 500 K) respectively, thereby confirming ZTE in the material. The obtained CTE values are compared to CTE values of various other oxide perovskites (see Table 5.1).

Table 5.1 CTE values for different oxide perovskite materials where α_l and α_V represent linear and volumetric CTE.

Compound	CTE ($\times 10^{-6}$ K^{-1})	Temperature range (K)	Reference
$BaZrO_3$	4.7 (α_l)	100 K-300 K	[295]
$BaZr_{0.6}Ti_{0.4}O_3$	≈ 13.37-22.96 (α_V) (Extracted from temperature -dependent Volume)	100 K-350 K	[206]
(Ba, Ca)(Ti, Zr)O_3	≈ 3.0-11.32 (α_l)	100 K-400 K	[296]
$BaSnO_3$	24.30 (α_V)	300 K	[297]
$SrTiO_3$	17.10 (α_V)	300 K	[297]
$SrVO_3$	17.70 (α_V)	300 K	[297]
$BaTiO_3$	17.80 (α_V)	300 K	[297]
$KNbO_3$	7.00 (α_V)	300 K	[297]
NNBCT05	≈ 9.51-20.05 (α_V) (Extracted from temperature -dependent Volume)	8 K-100 K	[298]
KBST20	**0.255-5.75 (α_l), 0.765-17.25 (α_V)**	**9 K-500 K**	**Present work**

NTE/ZTE in ferroelectric materials is observed due to high ferroelectricity resulting from the strong covalent character of *A*–O and(or) *B*–O bonds, referred to as ferroelectrostriction [19]. Ferroelectrostriction leads to volume gain at low temperatures, often referred to as the Ferroelectrovolume Effect (FVE) [19, 284]. Here, for KBST20 ceramics, the observed volume gain at low temperatures (see Fig. 5.1(e)) is quantitatively described by using a recently evolved quantifier known as spontaneous volume ferroelectrostriction (SVFS) ω_S [19, 280, 299]:

$$\omega_s = \frac{V_{\text{exp}} - V_{\text{nm}}}{V_{\text{nm}}} \times 100\% \tag{5.2}$$

where V_{exp} and V_{nm} correspond to experimental and nominal volumes, respectively. V_{nm} is the extrapolated value of volume obtained after fitting the Debye-Gr*ü*neisen equation

given follows:

$$V(T) \cong V_0 + 9K\gamma k_B NT\frac{T^3}{\theta_D^3}\int_0^{\theta_D/T}\frac{x^3}{e^x-1}dx \tag{5.3}$$

where V(T) is unit cell volume at temperature T, V_0 is unit cell volume at 0 K, γ is Grüniesen parameter, K is isothermal compressibility, k_B is Boltzmann constant, N is number of atoms in the primitive unit cell, and θ_D is the Debye temperature [17]. The equation is used to fit the experimental volume data in the temperature range 380 K $\leq T \leq$ 500 K as the deviation starts from Burns temperature ($T_B \approx$ 380 K). The Debye temperature (θ_D) and volume at 0 K (V_0) comes out to be 220 K and 61.986 Å^3 respectively. The experimental volume deviates from nominal volume (obtained from fitting), demonstrating a volume gain for KBST20.

Large values of SVFS result from high ferroelectrostriction, which leads to NTE/ZTE in the material [19, 299]. Figure 5.1(f) depicts SVFS as a function of temperature for KBST20. It is clearly evident from the figure that the SVFS increases ($\omega_S \approx 0.3\%$ at 9 K) with the decrease in temperature, thereby suggesting ZTE.

5.3.2 Dielectric and P-E loop analysis

Figure 5.3(a) depicts the variation of dielectric permittivity (ε') and loss ($tan\delta$) as a function of temperature (105 K$\leq T \leq$ 650 K). The ε' and tanδ exhibit observable contributions from electrical conductivity or space charge at low frequencies for high temperatures (see Fig. 5.3(a)) [22]. We observe a broad and diffuse dielectric peak with strong frequency dispersion ($\Delta T \approx$ 27 K) and dielectric maxima ($\varepsilon_{max} \approx$ 1708 at 10 kHz) near the room temperature ($T_m \approx$ 315 K) (see Fig. 5.3(b)). The diffuse broad peak, frequency dispersion, and an invariant long-range symmetry throughout are the relaxors' signature [5, 59, 117, 137]. Moreover, the dielectric permittivity curve deviates from the Curie-Weiss law for materials exhibiting diffuse phase transitions (DPT) and (or) relaxor behavior [5, 22, 117].

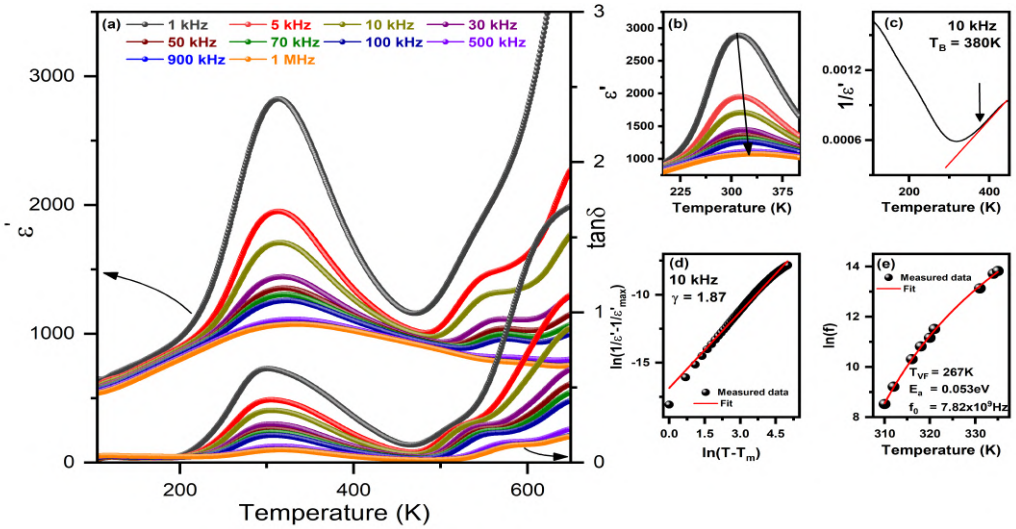

Fig. 5.3 (a) Temperature-dependent dielectric permittivity (ε') and loss ($\tan\delta$) plot at various frequencies, (b) the zoomed-up view of the observed frequency dispersion ($\Delta T \approx$ 27 K) with the same order of frequency as in 2(a), (c) the linear fitting of $ln(1/\varepsilon' - 1/\varepsilon'_{\max})$ vs. $ln(T - T_m)$ at 10 kHz for KBST20 ceramic, (d) Inverse of dielectric vs. temperature plot at 10 kHz, and (e) the Vogel-Fulcher law fitting for KBST20 ceramics.

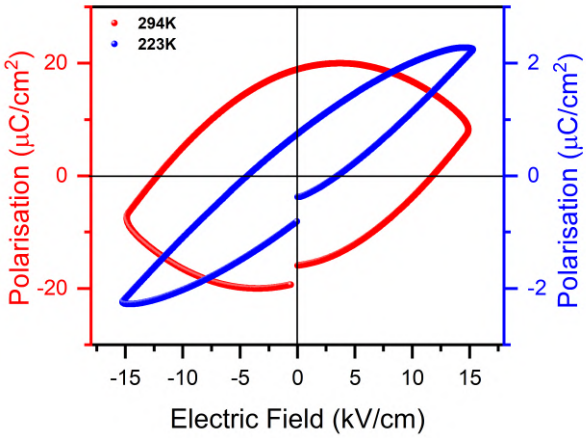

Fig. 5.4 Polarization vs Electric field response of KBST20 ceramics at 294 K and 223 K.

This deviation starts from Burn's temperature (T_B) and is determined from the inverse dielectric permittivity plotted as a function of temperature (*i.e.* $1/\varepsilon'$ vs T) (see Fig. 5.3(c)).

Owing to the relaxor properties of KBST20, the dielectric function can be fitted by the modified Curie-Weiss law formulated by Uchino and Nomura as [22, 300]:

$$\frac{1}{\varepsilon'} - \frac{1}{\varepsilon'_{\max}} = \frac{(T - T_{\mathrm{m}})^{\gamma}}{C} \tag{5.4}$$

where, C is the Curie constant, and γ is the diffusion exponent lying between $1 \leq \gamma \leq 2$. Here, $\gamma = 1$ corresponds to normal ferroelectrics, and $\gamma = 2$ corresponds to an ideal relaxor [22, 300]. The value of γ obtained after fitting the modified Curie-Weiss law is 1.87 (see Fig. 5.3(d)), which also suggests the relaxor behavior of the material. The relaxor properties in KBST20 are induced due to the presence of the heterovalent character of ions and ionic radii mismatch of *A*-site ($r_{Ba^{2+}}$ = 161 pm, $r_{Sr^{2+}}$ = 144 pm, $r_{K^{1+}}$ = 164 pm, $r_{Na^{1+}}$ = 139 pm) and *B*-site ($r_{Ti^{4+}}$ = 60.5 pm, $r_{Nb^{5+}}$ = 64 pm) [117, 148, 289]. Various theoretical models have been reported to explain the complex relaxor physics. Most of them suggest the presence of polar ordering in the form of PNR at short-ranges exhibiting lower symmetry than that at long-ranges [22, 59, 301]. The PNRs start to grow at T_{B}, and with the decrease in temperature, the intra-polar interactions (*i.e.*, interaction among dipoles in a polar nano region) increase, leading to the increase in the size of PNRs [22, 142, 302]. On further lowering the temperature, PNRs start to freeze at a certain temperature referred to as freezing temperature, which is determined by using the Vogel-Fulcher relation [143, 303]:

$$f = f_0 exp[-E_a/k_B(T_m - T_{\mathrm{VF}})] \tag{5.5}$$

where f and f_0 correspond to the measured frequency and pre-exponential factor, respectively, E_a is the activation energy, $\mathrm{k_B}$ is Boltzmann constant, T_m is the temperature corresponding to dielectric maxima, and T_{VF} is the freezing temperature below which the dynamics of PNRs freeze. Figure 5.3(e) shows the Vogel-Fulcher fit and various parameters *viz.*, T_{VF}, E_a, and f_0 obtained for KBST20. The freezing of PNRs takes place below T_{VF} leading to inter-polar interactions (*i.e.*, interactions among PNRs) [142], inferred from merging of temperature-dependent dielectric curves at different frequencies at low temperatures. This observation is supplemented by temperature-dependent hysteresis loops.

The shape of the hysteresis loop at room temperature (see Fig. 5.4) bears a resemblance to a linear lossy dielectric, indicating disorder within the system [290]. However, on lowering the temperature to 223 K (below T_{VF}) (see Fig. 5.4), the shape of the loop is relaxor-like [290]. This change in the shape of the loop with temperature is suggestive of enhanced cationic (polar) ordering at low temperatures.

Now, an intuitive crystallographic model for KBST20 has been proposed to correlate ZTE with the increase in cationic ordering at low temperatures. At room temperature, the material is in a relatively disordered state where a significant amount of rattling space is available for smaller Ti^{4+} cations by the random distribution of surrounding Nb^{5+} cations, which are relatively larger in size [286, 287]. In contrast, a much smaller rattling space is available at low temperatures due to cationic ordering [286, 287]. Moreover, in the disordered state, the *B*-site cations rattle without distorting the neighboring oxygen octahedra. However, in an ordered state, the motion of *B*-site cations is constrained, which transfers octahedral stress to adjacent oxygen octahedra, leading to ferroelectrostriction [286, 287]. Thus, we believe that the increase in correlations among ferroeletrostrictive PNRs results in zero thermal expansion at low temperatures. Further, we have analyzed the temperature-dependent Raman data to comprehend the ZTE observed for KBST20 at low temperatures.

5.3.3 Raman scattering analysis

The presence of short-range atomic ordering in the long-range cubic phase is determined by temperature-dependent Raman spectroscopic analysis. Here, the host ceramic *viz.*, KNN50 is reported to possess a monoclinic structure with *Pm* space group at short-ranges as well as long-ranges with variations in lattice parameters/volume [56, 168, 171, 241, 304]. The room temperature Raman spectra for KBST20 shows Raman peaks similar to what has been reported earlier for KNN50, suggesting the presence of polar monoclinic distortions

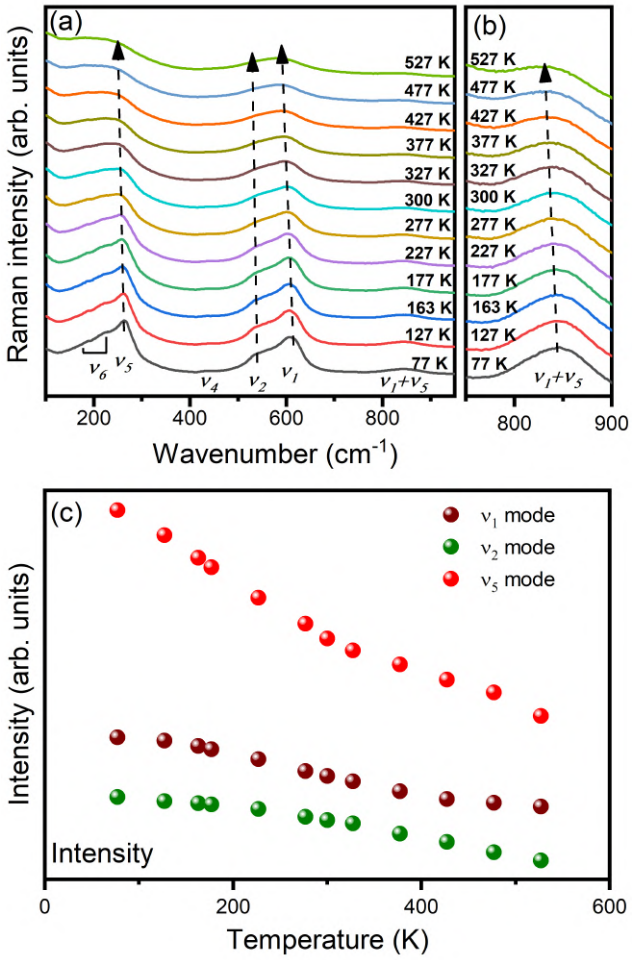

Fig. 5.5 (a) Temperature-dependent Raman data for KBST20 ceramic, (b) zoomed-up view of polar peak ($\nu_1 + \nu_5$) as a function of temperature, (c) the temperature-dependent intensity observed for prominent Raman modes (ν_1, ν_2, and ν_5).

at short-ranges for KBST20 [168, 241]. Figure 5.5(a) depicts the evolution of temperature-dependent Raman spectra for KBST20 ceramics with prominent peaks *viz.*, ≈245-265 cm^{-1} (ν_5), ≈525-553 cm^{-1} (ν_2), ≈585-610 cm^{-1} (ν_1), and ≈830-845 cm^{-1} ($\nu_1 + \nu_5$) present throughout. The peaks below 200 cm^{-1} correspond to translational modes of *A*-site cations similar to what has been observed for $NaNbO_3$ and $KNbO_3$ [305]. The existence of polar distortions in BO_6 octahedra is clearly evident by the presence of ($\nu_1 + \nu_5$) peak in the Raman spectra [306, 307]. This peak persists throughout the studied temperature range

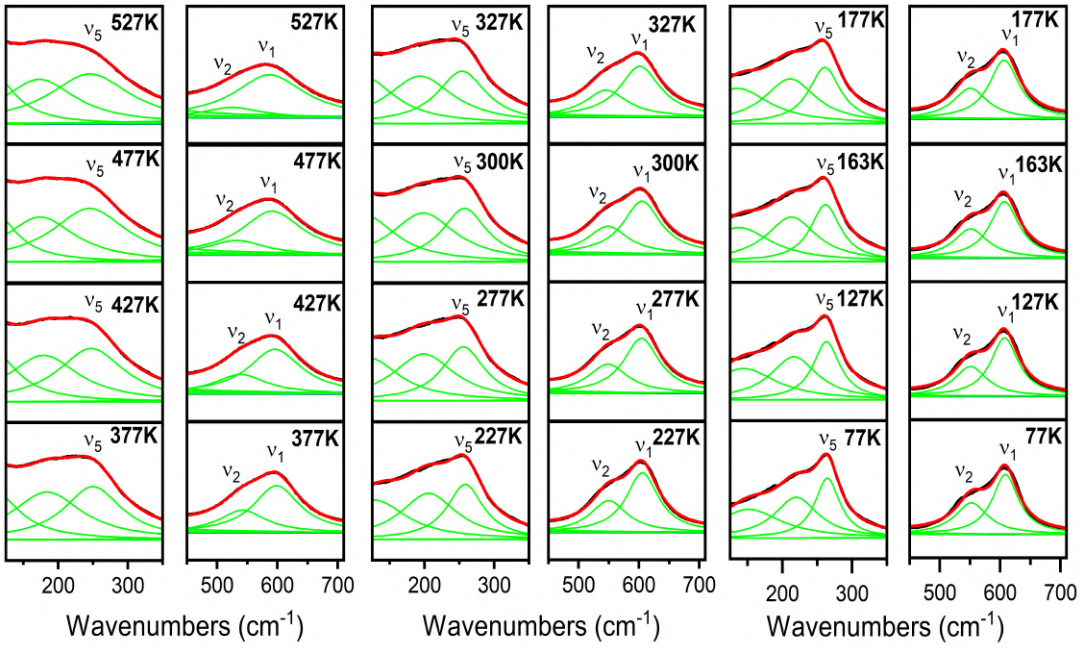

Fig. 5.6 Deconvolution of Raman peaks *viz.*, ν_5 ($\approx 245-265$ cm^{-1}), ν_1 and ν_2 ($\approx 500-700$ cm^{-1}), for the temperature range 77 K $\leq T \leq$ 527 K.

(77 K $\leq$ T $\leq$ 527 K) (see Fig. 5.5(b)], confirming the presence of polar clusters up to the highest temperatures. Thus, the ferroelectrostrictive behavior observed for KBST20 having average cubic symmetry at long-ranges has been attributed to the correlations among ferroelectrostrictive polar clusters (PNRs). All the Raman peaks broaden with the increase in temperature, inferring thermal disorder in the system [202, 308]. Figure 5.5(c) depicts the intensity variation of prominent Raman peaks as a function of temperature, which is calculated after fitting Raman peaks using Lorentz function (see Fig. 5.6). The intensity of Raman peaks depends on various factors *viz.*, polarizability, presence of polar phase, etc [202, 308].

Here, we can see that the intensity of Raman modes increases (see Fig. 5.5(c)) with the decrease in temperature inferring the increase in polar phased regions at low temperatures *i.e.*, due to enhanced inter/intra polar interactions [142]. The enhanced short-range polar ordering with the increase in correlations (inter/intra polar cluster interactions) among

PNRs at low temperatures are held responsible for ferroelectrostriction, consequently resulting in zero thermal expansion [142, 302] in synthesized Pb-free smart material *viz.*, KBST20.

5.4 Conclusions

In conclusion, we have synthesized Pb-free relaxor ferroelectrics *i.e.*, KBST20 exhibiting zero thermal expansion (ZTE) for a wide temperature range ($T \leq 100K$). The temperature-dependent volume of KBST20 deviates from linear behavior *i.e.*, PTE below Burns temperature showing a significant volume gain at low temperatures, which has been attributed to the correlations among ferroelectrostrictive polar nanoregions (PNRs). The ZTE has been quantified using the linear coefficient of thermal expansion (CTE), which is in the range of 0.255-5.75 $\times 10^{-6}$ K^{-1} (9 K-500 K). The relaxor properties of KBST20 have been analyzed using temperature-dependent dielectric data, demonstrating a relatively high relaxation ($\Delta T \approx 27$ K) compared to an earlier report on KBT20 ($\Delta T \approx 6$ K) [15]. Owing to relaxor properties, the structures of KBST20 at long- and short-ranges were analyzed using temperature-dependent neutron diffraction and Raman scattering data, respectively. A centrosymmetric cubic structure was found to be stable at long-ranges for 9 K$\leq T \leq$ 500 K. On the other hand, polar monoclinic distortions were confirmed at short ranges. Moreover, the enhancement in the polar phased regions (PNRs) at low temperatures is inferred by the integrated analysis of the datasets obtained using various techniques. We believe that the enhancement in the correlations among the PNRs with decreasing temperature leads to thermally induced ferroelectrostriction, consequently resulting in zero thermal expansion of KBST20.

In the next chapter, we will explore the crystal structure at long/short ranges and associated properties as a function of composition (x) and temperature (T) for the other end of (1-x)KNN50-xBST10 for $0.90 \leq x \leq 1.00$.